

Contrast-enhanced imaging of SPIO-labeled platelets using magnetomotive ultrasound

Ava G Pope¹, Gongting Wu¹, Frances Y McWhorter^{2,5},
Elizabeth P Merricks³, Timothy C Nichols³, Tomasz J Czernuszewicz²,
Caterina M Gallippi² and Amy L Oldenburg^{1,2,4,6}

¹ Department of Physics and Astronomy, University of North Carolina at Chapel Hill, Chapel Hill, NC, 27599-3255, USA

² Joint Department of Biomedical Engineering, University of North Carolina at Chapel Hill, Chapel Hill, NC, 27599-7575, USA

³ Francis Owen Blood Research Laboratory, University of North Carolina at Chapel Hill, Chapel Hill, NC 27510, USA

⁴ Biomedical Research Imaging Center, University of North Carolina at Chapel Hill, Chapel Hill NC, 27599-7513, USA

E-mail: aold@physics.unc.edu

Received 24 May 2013, in final form 31 August 2013

Published 26 September 2013

Online at stacks.iop.org/PMB/58/7277


Abstract

The ability to image platelets *in vivo* can provide insight into blood clotting processes and coagulopathies, and aid in identifying sites of vascular endothelial damage related to trauma or cardiovascular disease. Toward this end, we have developed a magnetomotive ultrasound (MMUS) system that provides contrast-enhanced imaging of superparamagnetic iron oxide (SPIO) labeled platelets via magnetically-induced vibration. Platelets are a promising platform for functional imaging contrast because they readily take up SPIOs and are easily harvested from blood. Here we report a novel MMUS system that accommodates an arbitrarily thick sample while maintaining portability. We employed a frequency- and phase-locked motion detection algorithm based on bandpass filtering of the differential RF phase, which allows for the detection of sub-resolution vibration amplitudes on the order of several nanometers. We then demonstrated MMUS in homogenous tissue phantoms at SPIO concentrations as low as $0.09 \text{ mg ml}^{-1} \text{ Fe}$ ($p < 0.0001$, $n = 6$, t -test). Finally, we showed that our system is capable of three-dimensional imaging of a $185 \mu\text{L}$ simulated clot containing SPIO-platelets. This highlights the potential utility for non-invasive imaging of platelet-rich clots, which would constitute a fundamental advance

⁵ Currently in the Department of Biomedical Engineering at the University of California.

⁶ Author to whom any correspondence should be addressed.

in technology for the study of hemostasis and detection of clinically relevant thrombi.

 Online supplementary data available from stacks.iop.org/PMB/58/7277/mmedia

(Some figures may appear in colour only in the online journal)

1. Introduction

Platelets play an important role in the processes of hemostasis and thrombosis, which are closely linked to many blood diseases and conditions (Jurk and Kehrel 2005). The pathophysiological function of platelets is to actively respond to endothelial damage by forming a platelet-rich thrombus that inhibits blood flow (primary and secondary hemostasis), where the type of endothelial disruption dictates the clinical relevance of the thrombus. For example, occlusive thrombus formation often results from the rupture of a vulnerable atherosclerotic plaque, and is the leading cause of myocardial infarction and stroke. Importantly, pre-occlusive thrombosis complicating atherosclerosis, if properly diagnosed, may be attended to before becoming occlusive (Lloyd-Jones *et al* 2010). Alternatively, non-pathogenic hemostasis involves the formation of platelet-rich thrombi that halt internal hemorrhage (Becker 2008). Thus, platelet-rich thrombus formation is broadly relevant for diagnosing and studying cardiovascular disease (CVD) and trauma. Imaging technologies for detecting and longitudinally monitoring the development of platelet-rich thrombi would therefore greatly aid in the study and diagnosis of CVD and internal hemorrhage. In this paper, we address this need by a first demonstration of a non-invasive and portable magnetomotive ultrasound (MMUS) technique capable of contrasting platelet-rich clots formed from SPIO-labeled platelets.

The current clinical standard for detecting platelet-rich thrombi is x-ray angiography, and emerging imaging strategies are being developed using MRI, CT, and PET (Ciesiński and Caravan 2010, Sanz and Fayad 2008). Though these imaging modalities are helpful in diagnosing blood related diseases, ultrasonic imaging offers lower cost, portability, and avoids the radiation hazard associated with x-rays. Micrometer and submicrometer-sized bubbles have been extensively employed in ultrasonic imaging to provide molecularly-sensitive imaging to a wide variety of pathologies (Kaufman and Linder 2007, Ferrara *et al* 2007). Also, ultrasound radiation force methods have been developed to provide image-guided drug delivery via microbubble carriers (Lum *et al* 2006, Patil *et al* 2009, 2011). There are also emerging methods for molecular imaging with photoacoustic tomography using nanoparticles (Zerda *et al* 2010, Li *et al* 2008). Each of these techniques offers advantages and disadvantages in comparison to the proposed use of SPIO-labeled platelets. First, microbubbles provide bright field contrast, which enhances sensitivity to small vessels; in comparison, photoacoustic and magnetomotive contrast methods are darkfield, providing specific imaging of molecular imaging agents that can be overlaid onto the brightfield image. Second, traditional molecular imaging methods rely upon receptor-ligand binding of micro- and nanoparticles; in comparison, platelets are activatable and respond to their environment, presenting multiple types of tethering structures and changing shape to facilitate adhesion to sites of inflamed and damaged vascular endothelium (Jurk and Kehrel 2005).

At the same time, the recent development of novel imaging technologies like high speed confocal and wide-field microscopy (Falati *et al* 2002), intravital video microscopy (Furie and Furie 2005, Nishimura *et al* 2012), and nanoscale spectral CT molecular imaging (Pan *et al* 2010) provide high-resolution imaging of thrombus formation in small animals, including

longitudinal information on thrombus composition and physical structure. While these techniques have contributed significantly to our understanding of thrombosis and hemostasis, they are invasive and impractical for *in vivo* imaging in humans. Imaging technologies with the ability to non-invasively locate platelets in an *in vivo* environment could be employed both as a research imaging tool in large animal models, and provide biomedical imaging in humans for detection of internal vascular damage and clinically silent or pre-occlusive thrombosis.

Platelets have been shown to readily take up nanoparticles via immune processes (White *et al* 1999) and when labeled with imaging contrast agents, provide a platform for functional imaging. Since the 1970s, platelets have been used as radio labeled contrast agents in gamma ray imaging for the study of blood related diseases (Fuster *et al* 1979). In recent work, we showed that platelets exhibit an affinity for the uptake of superparamagnetic iron oxide (SPIO) contrast agents, enabling imaging by magnetomotive optical coherence tomography (MMOCT) (Oldenburg *et al* 2010, 2012).

Magnetomotive imaging is a method for contrasting magnetically labeled agents that are non-echogenic by detecting the motion of echogenic materials to which they are mechanically coupled in response to an applied magnetic field (in otherwise non-magnetic tissue), which was first demonstrated using OCT (Oldenburg *et al* 2005a), and later demonstrated in ultrasound (Oh *et al* 2006). The amplitude of the magnetomotion depends upon the particle distribution, particle magnetization, magnetic field strength and gradient, and the mechanical properties of the surrounding medium (Oldenburg *et al* 2005b). Given that OCT offers limited penetration depth ($\sim 1\text{--}2$ mm), and that OCT and ultrasound are both reflection-based, interferometric imaging techniques, this manuscript represents the translation of our phase-sensitive techniques for magnetomotive imaging of SPIO-platelets to an ultrasound platform. This extends the imaging penetration depth by over an order of magnitude, broadening the potential application base to include non-invasive, *in vivo* imaging of peripheral vasculature (within $\sim 2\text{--}3$ cm of the surface).

MMUS was first demonstrated using standard Doppler techniques for detection of SPIO uptake in *ex vivo* mouse liver (Oh *et al* 2006). Doppler-based MMUS was further developed to image uptake in live macrophages embedded in agar (Mehrmohammadi *et al* 2007). Advances toward more robust MMUS motion detection algorithms were developed to enhance the signal-to-noise ratio (SNR) (Holst *et al* 2010) and efforts toward quantitative MMUS have been made (Evertsson *et al* 2011). Furthermore, different methods of magnetic field delivery and SPIO optimization have been explored (Mehrmohammadi *et al* 2011c, 2011a, 2011b). The coupling of MMUS with photo-acoustic tomography using dual-function nanoparticles has also been demonstrated (Qu *et al* 2011).

Here we report further advances in MMUS technology toward clinical application and functional imaging of platelets. We have designed a novel magnetic field delivery system that allows for open air imaging of arbitrarily thick samples, which is readily translatable to large animal and human studies. The MMUS signal is extracted with high sensitivity and specificity using a frequency- and phase-locked method translated from our previous work in MMOCT (Oldenburg *et al* 2008), and similar to other MMUS work by Holst *et al* (2010). The method presented here provides several advantages: (1) it rejects noise outside the frequency passband (frequency-locking), (2), it rejects background motion that is out-of-phase with the driving force (phase-locking), and (3) it further suppresses low-frequency noise (such as $1/f$ noise) by use of the differential phase. With this novel MMUS system we show that we can detect motion in homogenous tissue phantoms and in small platelet-rich clot-like inclusions at physiologically feasible concentrations. This lays a foundation for translation to *in vivo*

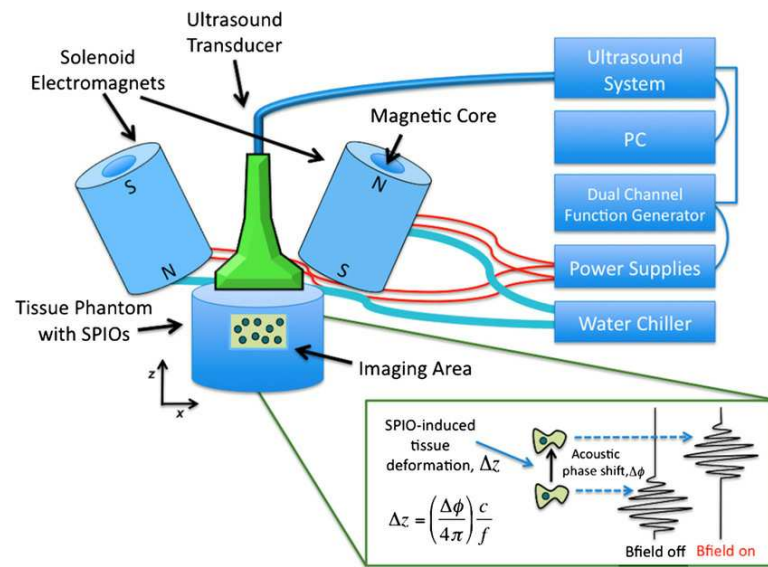


Figure 1. Cartoon diagram of the open-air magnetomotive ultrasound (MMUS) system. The green inset illustrates the acoustic phase shift arising from magnetomotion in the sample, where Δz is tissue displacement, c is speed of sound in tissue, and f is acoustic frequency.

experiments that can provide fundamental knowledge about hemostasis arising from trauma and thrombosis.

2. Materials and methods

2.1. Open-air MMUS system setup

The open-air MMUS system (figure 1) is comprised of an UltraSonix SonixTouch Research machine with a L14-5/38 linear array transducer operating at a center frequency of 10 MHz. The ultrasound transducer is mounted between a pair of custom, water-jacketed solenoid electromagnets that provide a temporally modulated magnetic field gradient during imaging. An arbitrary waveform generator signals two identical power supplies (Kepco model ATE-75-15M, 1000 Watt), which power the two electromagnets to produce the magnetic field. The ultrasound system triggers the waveform generator so that the electromagnets begin generating a field at the same instance the system begins collecting ultrasound data. This triggering allows us to phase filter mechanical noise from the MMUS signal. The electromagnets have cores made from laminated layers of grain-oriented electrical steel (ATI Allegheny Ludlum), and are in a solenoid configuration composed of 20 gauge magnet wire wound with inner and outer radii of 3.5 cm and 6.8 cm, respectively, and a height of 10.7 cm. To produce a maximum gradient force they are operated in an anti-parallel configuration and positioned directly above the tissue phantoms at a tilt angle of 25°. The coil dimensions, wire gauge, and tilt angle were chosen using a multi-dimensional optimization algorithm to model and maximize the resulting magnetic gradient force within the imaging area. The imaging apparatus is mounted on a vibration isolation table to reduce ambient mechanical noise. The sample and transducer holders are also mechanically decoupled from the electromagnets to avoid

detection of mechanical vibrations of the electromagnets. At the same time, the transducer and electromagnets are co-mounted on a 1-d axial (z) translation stage to enable positioning of the transducer onto the sample while maintaining alignment of the electromagnets in the B-mode (x - z) plane. The sample holder is mounted on a 1-d elevational (y) translation stage to allow for 3-d MMUS imaging.

2.2. Data collection and analysis

Each MMUS data set consisted of two 8 s sets of ultrasound data (2-d B-mode style RF acquisition) acquired using ‘RF mode’ on the SonixTouch for off-line processing (61.667 frames per second). One set was taken while the B-field was modulated at 2.0031 Hz (the frequency of which was chosen to ensure proper operation of Goertzel algorithm described below) and one set taken with the B-field completely off. The field-off data allows for subtraction of ambient noise during processing. For 3-d imaging, the sample was translated in elevation while the transducer and magnets maintained fixed positions.

We then employed a slow time phase-sensitive motion detection algorithm. It is similar to that previously used in magnetomotive OCT (Oldenburg *et al* 2008), and similar to a recently reported frequency- and phase-locked method for MMUS (Holst *et al* 2010) with the exception that our method employs slow time differential phase to suppress $1/f$ noise. First, we write the time-varying magnetic gradient force as:

$$F(t) \propto \exp(i\omega_{\text{magnet}}t + i\varphi_{\text{magnet}}),$$

where ω_{magnet} is the magnetic oscillation frequency, t is the time elapsed since the magnet was switched on, and φ_{magnet} is the phase of the magnetic oscillation at $t = 0$. Once it has reached a steady-state, the magnetically-induced axial (z) displacement of the tissue can be written as:

$$\Delta z(\vec{r}, t) = z(\vec{r}, t) - z(\vec{r}, 0) = A(\vec{r}) \exp(i\omega_{\text{magnet}}t + i\varphi_{\text{magnet}}),$$

where A is the vibration amplitude and \vec{r} corresponds to the position of each pixel in the image. The size of A is proportional to the SPIO loading and tissue compliance (Oldenburg *et al* 2008). Finally, the magnetically-induced acoustic phase shift will be:

$$\Delta\phi_{\text{induced}}(\vec{r}, t) = \phi(\vec{r}, t) - \phi(\vec{r}, 0) = \left(\frac{4\pi f}{c}\right)A(\vec{r}) \exp(i\omega_{\text{magnet}}t + i\varphi_{\text{magnet}}),$$

where c is the speed of sound in tissue, and f is the acoustic frequency. Here we assume that f is constant, although a more accurate estimation can be made by accounting for its depth-dependence (Loupas *et al* 1995). We expect this effect to induce $<5\%$ error in the measurements reported in this study.

Ultimately, A represents the SPIO-induced signal that we wish to extract from the acoustic measurements. To accomplish this, we first acquired beamformed RF data as above, and in post-processing, we computed the Hilbert transform of the entire 8 s data set in slow time to extract the complex analytic ultrasound signal. The phase (argument) of this complex analytic signal is the measured acoustic phase, which can be written as:

$$\phi_{\text{measured}}(\vec{r}, t) = \Delta\phi_{\text{induced}}(\vec{r}, t) + \phi(\vec{r}, 0) + N(\vec{r}, t),$$

where N represents a noise term. We then computed the differential phase from successive time samples:

$$\frac{\partial\phi_{\text{measured}}(\vec{r}, t)}{\partial t} = \frac{\phi_{\text{measured}}(\vec{r}, t + \Delta t) - \phi_{\text{measured}}(\vec{r}, t)}{\Delta t},$$

which can then be written in terms of our magnetically induced signal and noise as:

$$\frac{\partial\phi_{\text{measured}}(\vec{r}, t)}{\partial t} = \left(\frac{4\pi f\omega_{\text{magnet}}}{c\Delta t}\right)A(\vec{r}) \exp\left(i\omega_{\text{magnet}}t + i\varphi_{\text{magnet}} + i\frac{\pi}{2}\right) + N'(\vec{r}, t).$$

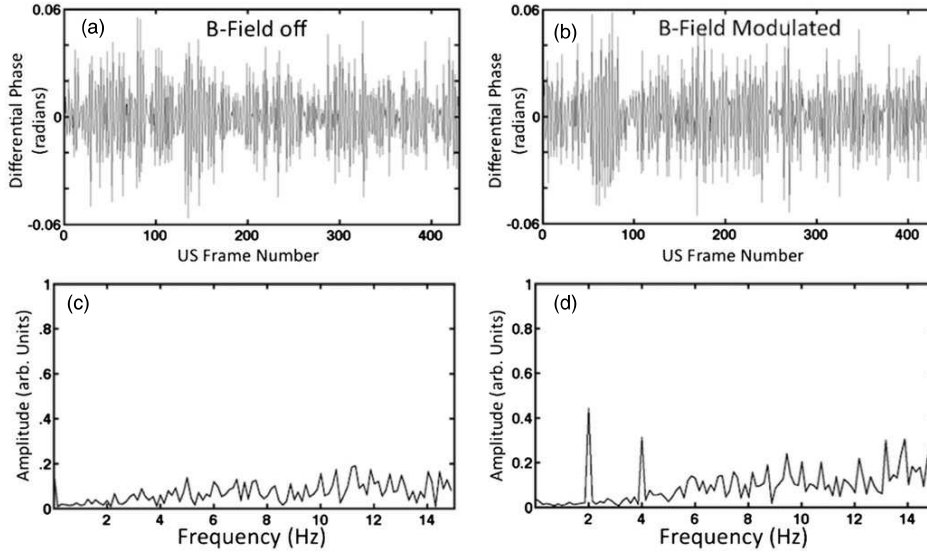


Figure 2. Example of data processing applied to a single pixel for detection of magnetically induced motion at 2 Hz in a homogeneous SPIO phantom. (a) and (b) show plots of the differential phase versus time. (c) and (d) illustrate the amplitudes from the corresponding Fourier transforms of the differential phase plots. Note that the 2 Hz peak only appears when the B-field is modulated. The second harmonic at 4 Hz is expected due to the square-law dependence of magnetic gradient force with the magnet current, although harmonics may also arise from other nonlinearities such as viscoelasticity.

For convenience we will neglect the constant terms in front of A . We then acquire the temporal Fourier transform of the differential phase which becomes:

$$F\left(\frac{\partial\phi_{\text{measured}}(\vec{r}, t)}{\partial t}\right) = A(\vec{r}) \exp\left(i\varphi_{\text{magnet}} + i\frac{\pi}{2}\right) \delta(\omega - \omega_{\text{magnet}}) + N'(\vec{r}, \omega),$$

where δ is the Dirac delta function. The amplitude of this Fourier spectrum for representative data is shown in figure 2.

In order to filter the signal at the magnet oscillation frequency, the Goertzel algorithm was used as it is a computationally efficient method for computing a single Fourier component from a discrete Fourier transform (Proakis and Manolakis 1996). This was applied to each 8 s data set to extract the Fourier component of the differential phase at ω_{magnet} . This Fourier component can then be written as $\tilde{S}(\vec{r})$ as follows:

$$\begin{aligned}\tilde{S}_{\text{Bon}}(\vec{r}) &= A(\vec{r}) \exp\left(i\varphi_{\text{magnet}} + i\frac{\pi}{2}\right) + N'(\vec{r}, \omega_{\text{magnet}}), \\ \tilde{S}_{\text{Boff}}(\vec{r}) &= N'(\vec{r}, \omega_{\text{magnet}})\end{aligned}$$

where we write expressions for the signals obtained with the magnetic field on and off, indicated as subscripts *Bon* and *Boff*, respectively. We then apply a cosine phase filter of the following form:

$$S_{\text{filt}}(\vec{r}) = |\tilde{S}(\vec{r})| \left(\frac{\cos(\arg(\tilde{S}(\vec{r})) - \varphi_{\text{magnet}} - \pi/2) + 1}{2} \right).$$

This selects the motion in phase with the oscillating magnetic field (Oldenburg *et al* 2008). For the case of more viscous samples (causing an additional phase lag) the reference phase term,

φ_{magnet} , may be modified to maximize detection of the desired motion. Finally, for rendering of MMUS contrast images we then display the value of $S_{\text{Bon, filt}}(\vec{r}) - S_{\text{Boff, filt}}(\vec{r})$. To generate an image-averaged measure of the magnetomotive signal, the SNR was computed from the ratio ($S_{\text{Bon, filt}}(\vec{r})/S_{\text{Boff, filt}}(\vec{r})$). For SPIO inclusions, the SNR was calculated for a manually selected region isolating the inclusion. As shown in supplemental material (supplementary data are available from stacks.iop.org/PMB/58/7277/mmedia), with this slow time frequency- and phase-sensitive method we can detect sub-resolution motion on the order of a few nanometers.

2.3. Magnetic field and force characterization

To obtain the largest possible SNR in MMUS it is necessary to maximize the z-component of the magnetic gradient force, F_z , produced by the electromagnets. To characterize this force, we measured the horizontal (x) and vertical (z) components of the magnetic field produced by the electromagnets within the imaging area of interest using an FW Bell 5180 Gauss/Tesla meter with an STD18-0404 probe that has a 0.38 mm diameter active sensor area. According to the following equation: $F_z \propto B_x(dB_x/dz) + B_y(dB_y/dz) + B_z(dB_z/dz)$, we computed a map proportional to the z component of force on SPIOs in the tissue phantom (see figure 4(g)). (Note that the magnitude of the force depends upon the field-dependent volume magnetization $\vec{M}(\vec{B})$ of the SPIOs according to $\vec{F} = (\vec{m} \cdot \nabla)\vec{B}$, where \vec{m} is the dipole moment of the particles given by $\vec{m} = \vec{M}V$, and V is particle volume.) After testing the magnets in both parallel and anti-parallel configurations it was found that anti-parallel polarizations produced the maximum force within the imaging area. It is interesting to note that, for the anti-parallel configuration, the predominant contribution to F_z is from the $B_x(dB_x/dz)$ (transverse) term. Correspondingly, all MMUS data was collected with the magnets in the anti-parallel configuration with an average field of 0.05 T and gradient of 0.09 T/m within the imaging area. While our electromagnets were designed to accommodate up to a 5 cm depth to match that of our ultrasound system, different electromagnet designs could be employed to deliver magnetic field gradients to larger depths.

2.4. SPIO-labeled platelet preparation

Platelets were harvested from fresh blood drawn in acid citrate dextrose anticoagulant solution from three-year-old normal female pigs at the Francis Owen Blood Research Laboratory according to approved protocols of the Institutional Animal Care and Use Committee at the University of North Carolina at Chapel Hill. We followed a modified version of a protocol developed by Aurich *et al* (2012). First, whole blood was centrifuged (100 g, room temperature, 20 min) to separate platelet rich plasma (PRP). The platelet concentration of PRP was determined by cell counter (SCIL Vet animal blood counter calibrated for pig cells) and 2 ml of red blood cells were set aside for later use in platelet rich clot formation. Platelets were then pelleted by spinning in a fixed-angle centrifuge at 800 g for 8 min. The platelet poor plasma was decanted from the pellets and stored on ice for later use.

For SPIO labeling, platelet pellets were resuspended in citrated saline (CS) to form a stock platelet solution and then further diluted with CS to a final concentration of 50×10^6 platelets/ml and either 0.5 mg Fe/ml SPIOs (Ocean Nanotech 10 nm, SHP 10–50) or no SPIOs as a control. These were incubated at 37 °C for 1 h 20 min. (At this point, samples were taken for visual evaluation of uptake by transmission electron microscopy (TEM): 400 μ L of SPIO-platelets and control platelets were fixed in 1% glutaraldehyde for 30 min and pelleted at 400 g for 15 min, then overlaid with 2% glutaraldehyde and taken to Microscopy Services Laboratory-UNC School of Medicine.) SPIO-platelets were

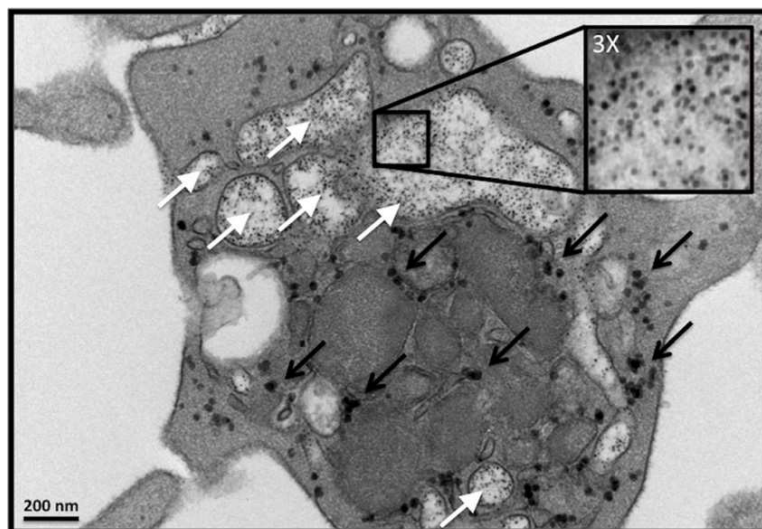


Figure 3. Transmission electron micrograph of an SPIO-labeled platelet. White arrows indicate areas of SPIO uptake while black arrows distinguish glycogen. Magnified inset shows the uptake individual SPIOs.

then pelleted (800 g, room temperature, fixed angle, 8 min) and supernatant containing free SPIOs was removed. It was verified that a control solution with only SPIOs exhibited no pelleting under these conditions. SPIO-platelets were re-suspended with 1 ml of CS for further analysis and phantom preparation. 100 μ l of both platelet solutions were then analyzed for Fe content by mass spectrometry (ICPMS, Mass Spectroscopy Facility, UNC Department of Chemistry).

2.5. Phantom preparation

We employed homogeneous tissue phantoms to determine the SPIO concentration-dependence of MMUS, and phantoms with an inclusion to study the spatial response of our system. See supplemental materials (supplementary data are available from stacks.iop.org/PMB/58/7277/mmedia) for detailed phantom preparation methods.

3. Results and discussion

3.1. SPIO uptake in platelets

TEM imaging of an SPIO-labeled platelet, (figure 3), reveals the presence of hundreds of SPIOs within the surface-connected open canalicular system of the platelet. SPIO uptake in platelets was quantified by mass spectrometry. It was found that each of the labeled platelets contains, on average, 140 fg of Fe, which is comparable to our previously reported efforts under varying conditions (table 1), although somewhat smaller than that reported by Aurich *et al* (2012). Further investigation is needed to understand how the differences in SPIO size, SPIO coating, incubation concentrations, platelet source, and platelet/SPIO separation methods relate to differences in platelet iron uptake.

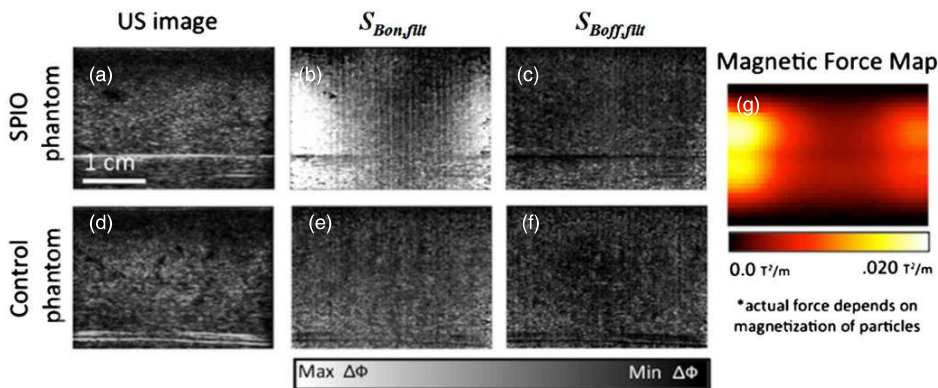


Figure 4. Imaging of homogeneous tissue phantoms (top row: 0.3 mg Fe/mL SPIO phantom, bottom row: control). (a) and (d) Representative ultrasound images. (b) and (e) MMUS images (represented by parameter S_{fill} calculated as described in section 2.2) obtained with the magnetic field modulated at 2 Hz, and (c) and (f) corresponding MMUS images with the magnetic field off. White corresponds to areas of maximum acoustic phase shift while black corresponds to no motion. (g) Map of the z -component of the magnetic gradient force within the US imaging area. As expected, the force field pattern matches that of the magnetomotive displacement observed in the SPIO field-on image of panel (b).

Table 1. Summary of platelet SPIO uptake experiments.

Citation	Particle coating	Hydrodynamic size (nm)	Platelet source	Separation method ^a	Final loading (fg Fe/platelet)
Oldenburg <i>et al</i> 2010	Dextran	30–40	Human	Size exclusion chromatography	43
Oldenburg <i>et al</i> 2012	Dextran	30–40	Human	Centrifugation	217
Aurich <i>et al</i> 2012	Carboxy-dextran	45–60	Human	Centrifugation	2000
This work	CO-OH	18–20	Porcine	Centrifugation	140

^a Separation of platelets from excess SPIOs.

3.2. MMUS of homogeneous tissue phantoms

Figure 4 shows representative US and MMUS images of a 0.3 mg Fe ml⁻¹ phantom in comparison to control. We found that MMUS contrast is only apparent in the SPIO phantom in the presence of a modulating magnetic field. There is some inhomogeneity in the MMUS image that may be explained by inhomogeneities of the magnetic field and field gradient in the imaging area of interest. As shown in panels (b) and (g) of figure 4, the MMUS signal pattern is strongly correlated with that of the force field. The force is somewhat concentrated near the axes of the electromagnet cores, while slightly stronger forces observed on the left side of the images may be attributed to slight inconsistencies between our two custom-made electromagnets. Horizontal lines near the bottom of the images are caused by acoustic interference patterns due to back reflection from the bottom of the phantom molds.

MMUS was performed on homogeneous phantoms of varying SPIO concentration. Data displayed in figure 5 demonstrates that the SNR of our MMUS system monotonically increases over SPIO concentrations ranging from 0.091 mg Fe ml⁻¹ to 0.91 mg Fe ml⁻¹. Each data point

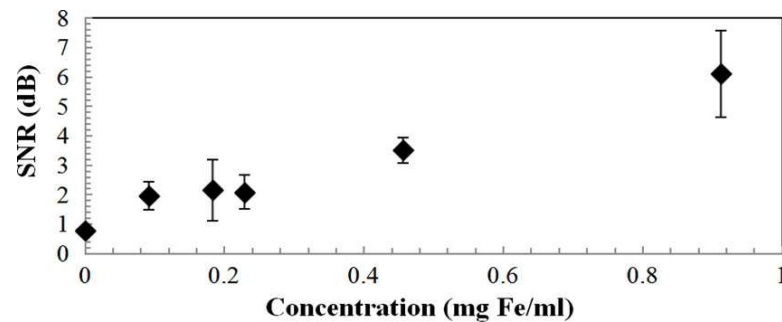


Figure 5. MMUS SNR versus SPIO concentration in homogenous tissue phantoms.

in figure 5 represents the mean and standard deviation of SNR for six MMUS images (three different locations, two acquisitions at each location). From this data, we see that the system can detect magnetically induced motion at a concentration of $.091 \text{ mg Fe ml}^{-1}$ in comparison to control ($p < 0.0001$, $n = 6$, t -test). In comparison, with closed MMUS systems Evertsson *et al* (2013) report a vibration amplitude sensitivity to $0.45 \text{ mg Fe ml}^{-1}$, and Mehrmohammadi *et al* (2007) show magnetomotive signal at concentrations of $0.07 \text{ mg Fe ml}^{-1}$.

In our experiments, non-random motion (SNR $\sim 0.7 \text{ dB}$) was observed in control phantoms that did not contain SPIOs. It is suspected that these motions arise from mechanical vibrations of the electromagnet cores that translate through the table to the graphite control samples. This hypothesis is consistent with the observation that the MMUS images of the graphite control phantoms exhibit an evenly distributed pattern that does not correspond to the magnetic gradient force map, unlike the MMUS signal in SPIO phantoms.

As another comparison, past MMOCT studies exhibited a sensitivity to SPIO laden platelets with final Fe content between $.060$ and $.070 \text{ mg Fe ml}^{-1}$ ($p < 0.0001$, $n = 9$, t -test) (Oldenburg *et al* 2010) and $0.027 \text{ mg Fe ml}^{-1}$ in homogeneous tissue phantoms (Oldenburg *et al* 2008). Interestingly, for MMOCT, sensitivity is ultimately limited by diamagnetically-induced motion of the water in the sample. This occurs when fields above the magnetic saturation point of SPIOs are used, which is a regime where diamagnetic motion increases nonlinearly while SPIO motion increases only linearly with increasing magnetic field (Oldenburg *et al* 2010). With this in mind, our open air magnetic field delivery system was designed to operate with field strengths below the saturation field of the SPIOs (0.1 – 0.2 Tesla). Consistent with this picture, we find no evidence that diamagnetic motion is significant in the open air MMUS.

To explore the vibration amplitude sensitivity we analyzed the motion of the lowest concentration sample and determined a nominal 3 dB sensitivity to harmonic vibrations on the order of 5 nm . A detailed explanation of this analysis may be found in the supplemental materials (supplementary data are available from stacks.iop.org/PMB/58/7277/mmedia). It is important to note that this vibration amplitude sensitivity is not equivalent to the true displacement sensitivity of the system, because *a priori* knowledge of the vibration waveform is used to extract the amplitude. Using data analysis techniques similar to ours, Evertsson *et al* (2013) report vibrations within phantoms on the order of 50 nm . Notably, in their work on harmonic motion detection in vibrating media using ultrasound, Urban *et al* (2008) report vibration amplitude sensitivity as low as 100 nm . Toward the goal of *in vivo* studies and clinical translation, we are encouraged that the vibration amplitude sensitivity of this open air MMUS system compares favorably to existing methods of harmonic motion detection.

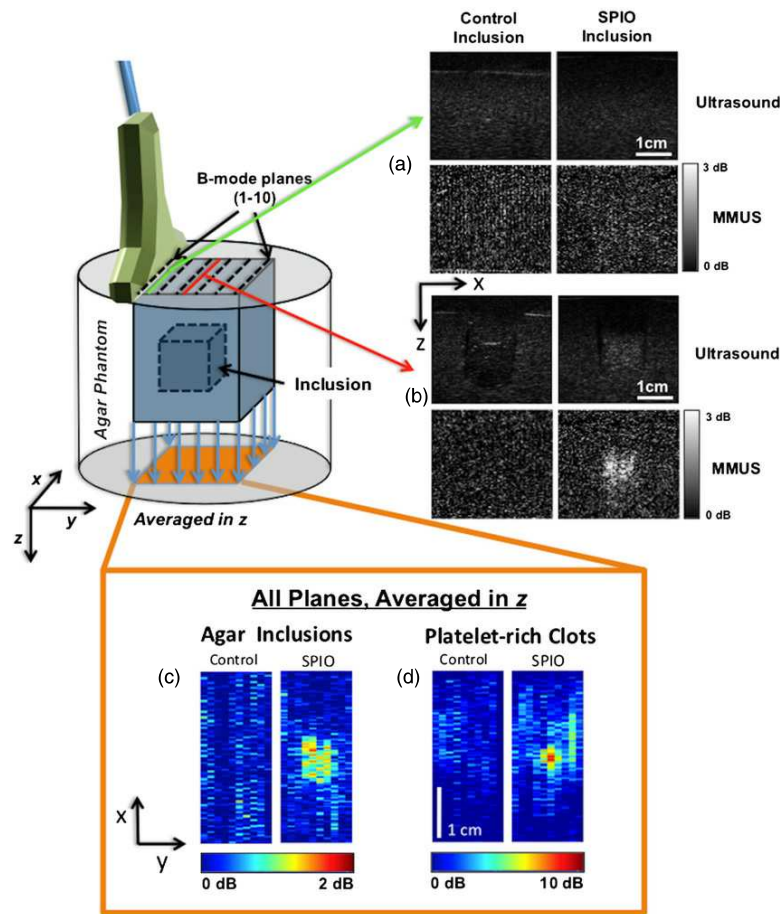


Figure 6. B-mode ultrasound and corresponding MMUS SNR images of graphite agar phantoms embedded with a graphite (control) inclusion, an SPIO-laden inclusion, a platelet (control) clot, or an SPIO-labeled platelet clot, as indicated. (a) Images for plane 1 (transducer not over inclusion). (b) Images for plane 4 (transducer over inclusion). (c) and (d) Projections of MMUS images (averaged in z) arising from elevational scans stepped in x . (c) Elevational scans of inclusions corresponding to the phantoms from (a) and (b). (d) Elevational scans of platelet rich clots (left = control clot, right = SPIO-labeled platelet clot). We observe a strong correspondence of MMUS contrast to the known SPIO inclusion and clot positions in both the y - z and x - y planes.

3.3. MMUS of phantoms with agar inclusions and platelet rich clots

To illustrate the potential of MMUS as a clinical tool for thrombus detection, we performed imaging of phantoms containing both SPIO-laden agar inclusions and SPIO-labeled platelet rich clots. The SPIO agar inclusion consisted of $1000 \mu\text{l}$ of $.91 \text{ mg Fe}$ and agar mixture, embedded $\sim 10 \text{ mm}$ beneath the phantom surface (figure 6) while the SPIO-labeled platelet rich clot had a volume of $185 \mu\text{l}$ with an iron concentration of $4.7 \text{ mg Fe ml}^{-1}$ (or $140 \text{ fg Fe/platelet}$). All together, the data shows that MMUS provides specific contrast only at the known positions of the SPIO-laden inclusions, including those comprised of SPIO agar and SPIO-labeled platelets in clots. In parts (a) and (b) of figure 6, it can be clearly seen that in

planes where neither inclusion exists (plane 1 the magnetomotive contrast is virtually non-existent. Conversely, the MMUS image plane located through the inclusion (plane 4) exhibits magnetomotive contrast only in the phantom with SPIOs in the inclusion, and is concentrated in the center of the image, corresponding to the known location of the inclusion.

Furthermore, in parts (c) and (d) we compare elevationally-scanned MMUS images of the agar inclusions to that of the platelet-rich clot inclusions. The iron concentration of the SPIO agar inclusion was $0.91 \text{ mg Fe ml}^{-1}$ while the iron concentration of the SPIO-labeled platelet rich clot was $4.7 \text{ mg Fe ml}^{-1}$. This may account for the accordingly larger SNR observed for the SPIO-labeled platelet rich clot (6.35 dB) in comparison to the SPIO agar inclusion (1.27 dB). SNR may also depend upon batch variability in the magnetization of SPIOs, and differences in the visco-elastic properties of the clots versus agar.

3.4. Discussion and future outlook

These results demonstrate that MMUS can locate SPIO-labeled platelets incorporated into clots within 3D tissue phantom volumes. Considering translation of this technology, *in vivo* platelet-rich thrombi can be comprised of a very high concentration of platelets. One study estimated that platelets comprise between 35–70% of thrombus by area (Sato *et al* 2005), corresponding to a concentration similar to that used in this study. The ability for MMUS to detect thrombosis *in vivo* will depend upon the fraction of platelets incorporated into the thrombus that are SPIO-labeled, the SPIO loading per platelet, and the total volume of the thrombus. Further development of SPIO-labeled platelets is also likely to improve existing loading efficiencies by gaining a better understanding of the effects of particle size, coating, and incubation conditions. The use of rehydratable, lyophilized (RL) platelets may also enable efficient harvesting, preparation, and storage of SPIO-RL platelets for MMUS imaging (Read *et al* 1995).

The image processing algorithm presented in this paper describes a phase- and frequency-locked method that operates in slow time upon the differential acoustic phase. This method rejects noise lying outside a very narrow passband, and further rejects noise that is out of phase with the driving magnetic field. This may be particularly robust when translating to *in vivo* imaging environments exhibiting other cyclical motions due to cardiopulmonary function. It will also reject non-harmonic motion, such as from SPIO-platelets that are not elastically bound, but are free within the blood volume. MMUS sensitivity may further benefit from the optimization of magnetic modulation frequency, which has begun to be addressed by Evertsson *et al* (2011). While higher frequencies would enable faster imaging rates, these will need to be balanced against possible tissue viscoelastic effects that damp vibrations, and the available frame rate and noise spectrum of the ultrasound hardware. Also, the choice of the optimum magnetic modulation frequency will depend strongly upon the *in vivo* noise spectrum from the aforementioned physiological motion artifacts. For this reason, we believe the next crucial step will be validating MMUS in an *in vivo* environment to more rapidly address challenges blocking the path to translation.

4. Conclusion

In summary, we have demonstrated a novel open-air MMUS system that enables contrast-enhanced imaging of SPIO-labeled platelet rich clots embedded in 3D tissue phantoms. Both the vibration amplitude sensitivity and SPIO concentration sensitivity of this MMUS system compare favorably with other closed MMUS systems, while additionally being capable of accommodating arbitrarily large samples for translational imaging. This poises the technology

for translation to *in vivo* animal imaging studies which will present new challenges for the technological advancement of MMUS. This research constitutes a first step toward contrast-enhanced imaging of SPIO-labeled platelets to study the mechanisms of thrombosis and to provide a sensitive clinical diagnostic for pre-occlusive thrombosis.

Acknowledgments

We would like to acknowledge Leandra Vicci for her help on the MMUS electromagnet design and Chase Dubois for his help with magnet characterization. This study was funded by the National Institutes of Health National Heart, Lung, and Blood Institute (R21HL109832, ALO, PI; R24HL63098, TCN, PI; T32HL069768, TJC, Nobuyo Maeda, PI; R01HL092944, CMG, PI), the Department of Defense Office of Naval Research (ONR DURIP N00014-10-1-0792, ALO, PI), the National Institutes of Health North Carolina Translational and Clinical Sciences Institute (UL1RR025747 with pilot grant 10KR61022 to ALO), the Department of Education GAANN Fellowship (P200A090135, AP), the National Institutes of Health Fellowship (5T90DA22857-04, FM), and startup funds at the University of North Carolina at Chapel Hill (ALO).

References

- Aurich K, Spoerl M-C, Furll B, Sietmann R, Greinacher A, Hosten N and Weitschies W 2012 Development of a method for magnetic labeling of platelets *Nanomedicine* **8** 537–44
- Becker R C 2008 Platelet biology: the role of platelets in hemostasis, thrombosis and inflammation *Platelets in Cardiovascular Disease* ed D L Bhatt (London: Imperial College Press) pp 1–36
- Ciesienki K L and Caravan P 2010 Molecular MRI of thrombosis *Curr. Cardiovasc. Imaging Rep.* **4** 77–84
- Evertsson M, Cinthio M, Fredriksson S, Olsson F, Persson H W and Jansson T 2011 Normalization of magnetic field effects: towards quantitative magnetomotive ultrasound imaging *Proc. IEEE Int. Ultrasonics Symp.* pp 775–8
- Evertsson M, Cinthio M, Fredriksson S, Olsson F, Persson H W and Jansson T 2013 Frequency- and phase-sensitive magnetomotive ultrasound imaging of superparamagnetic iron oxide particles *IEEE Trans. Ultrason. Ferroelectr. Freq. Control* **60** 481–91
- Falati S, Gross P, Merrill-Skoloff G, Furie B C and Furie B 2002 Real-time *in vivo* imaging of platelets, tissue factor and fibrin during arterial thrombus formation in the mouse *Nature Med.* **8** 1175–81
- Ferrara K, Pollard R and Borden M 2007 Ultrasound microbubble contrast agents: fundamentals and application to gene and drug delivery *Annu. Rev. Biomed. Eng.* **9** 415–47
- Furie B and Furie B C 2005 Thrombus formation *in vivo* *J. Clin. Invest.* **115** 3355–62
- Fuster V, Dewanjee M K, Kaye M P, Josa M, Metke M P and Chesebro J H 1979 Noninvasive radioisotopic technique for detection of platelet deposition in coronary artery bypass grafts in dogs and its reduction with platelet inhibitors *Circulation* **60** 1508–12
- Holst M, Cinthio M, Fredriksson S, Olsson F, Persson H W and Jansson T 2010 Phase-locked magnetomotive ultrasound imaging of superparamagnetic iron-oxide nanoparticles *Proc. IEEE Int. Ultrasonics Symp.* pp 1007–10
- Jurk K and Kehrel B E 2005 Platelets: physiology and biochemistry *Semin. Thromb. Hemost.* **31** 381–92
- Kaufman B A and Linder J R 2007 Molecular imaging with targeted contrast ultrasound *Curr. Opin. Biotechnol.* **18** 11–16
- Li P-C, Wang C-R C, Shieh D-B, Wei C-W, Liao C-K, Poe C, Jhan S, Ding A-A and Wu Y-N 2008 *In vivo* photoacoustic molecular imaging with simultaneous multiple selective targeting using antibody-conjugated gold nanorods *Opt. Express* **16** 18605–15
- Lloyd-Jones D, Adams R J and Brown T M *et al* 2010 Heart disease and stroke statistics—2010 update: a report from the American Heart Association *Circulation* **121** e46–215
- Loupas T, Powers J T and Gill R W 1995 An axial velocity estimator for ultrasound blood flow imaging, based on a full evaluation of the Doppler equation by means of a two-dimensional autocorrelation approach *IEEE Trans. Ultrason. Ferroelectr. Freq. Control* **42** 672–88
- Lum A F H, Borden M A, Dayton P A, Kruse D E, Simon S I and Ferrara K W 2006 Ultrasound radiation force enables targeted deposition of model drug carriers loaded on microbubbles *J. Control Release* **11** 128–34

- Mehrmohammadi M *et al* 2007 Imaging of iron oxide nanoparticles using magneto-motive ultrasound *Proc. IEEE Ultrasonics Symp.* pp 652–5
- Mehrmohammadi M, Oh J, Mallidi S and Emelianov S Y 2011a Pulsed magneto-motive ultrasound imaging using ultrasmall magnetic nanoprobe *Mol. Imaging* **10** 102–10
- Mehrmohammadi M, Qu M, Ma L L, Romanovicz D K, Johnston K P, Sokolov K V and Emelianov S Y 2011b Pulsed magneto-motive ultrasound imaging to detect intracellular accumulation of magnetic nanoparticles *Nanotechnology* **22** 415105
- Mehrmohammadi M, Yoon K Y, Qu M, Johnston K P and Emelianov S Y 2011c Enhanced pulsed magneto-motive ultrasound imaging using superparamagnetic nanoclusters *Nanotechnology* **22** 045502
- Nishimura S, Ichiro M and Nagasaki M *et al* 2012 *In vivo* imaging visualizes discoid platelet aggregations without endothelium disruption and implicates contribution of inflammatory cytokine and integrin signaling *Blood* **119** e45–56
- Oh J, Feldman M D, Kim J, Condit C, Emelianov S and Milner T E 2006 Detection of magnetic nanoparticles in tissue using magneto-motive ultrasound *Nanotechnology* **17** 4183–90
- Oldenburg A L, Crecea V, Rinne S A and Boppart S A 2008 Phase-resolved magnetomotive OCT for imaging nanomolar concentrations of magnetic nanoparticles in tissues *Opt. Express* **16** 11525–39
- Oldenburg A L, Gallippi C M, Tsui F, Nichols T C, Beicker K N, Chhetri R K, Spivak D, Richardson A and Fischer T H 2010 Magnetic and contrast properties of labeled platelets for magnetomotive optical coherence tomography *Biophys. J.* **99** 2374–83
- Oldenburg A L, Gunther J R and Boppart S A 2005a Imaging magnetically labeled cells with magnetomotive optical coherence tomography *Opt. Lett.* **30** 747–9
- Oldenburg A L, Toublan F J-J, Suslick K S, Wei A and Boppart S A 2005b Magnetomotive contrast for *in vivo* optical coherence tomography *Opt. Express* **13** 6597–614
- Oldenburg A L, Wu G, Spivak D, Tsui F, Wolberg A S and Fischer T H 2012 Imaging and elastometry of blood clots using magnetomotive optical coherence tomography and labeled platelets *IEEE J. Sel. Top. Quantum Electron.* **18** 1100–21
- Pan D *et al* 2010 Computed tomography in color: nanoK-enhanced spectral CT molecular imaging *Angew. Chem. Int. Ed. Engl.* **122** 9829–33
- Patil A V, Rychak J J, Allen J S, Klibanov A L and Hossack J A 2009 Dual frequency method for simultaneous translation and real-time imaging of ultrasound contrast agents within large blood vessels *Ultrasound Med. Biol.* **35** 2021–30
- Patil A V, Rychak J J, Klibanov A L and Hossack J A 2011 A real-time technique for improving molecular imaging and guiding drug delivery in large blood vessels: *in vitro* and *ex vivo* results *Mol. Imaging* **10** 238–47
- Proakis J G and Manolakis D G 1996 *Digital Signal Processing: Principles, Algorithms, and Applications* (Upper Saddle River, NJ: Prentice Hall) pp 480–1
- Qu M, Mallidi S, Mehrmohammadi M, Truby R, Homan K, Joshi P, Chen Y-S, Sokolov K and Emelianov S 2011 Magneto-photo-acoustic imaging *Biomed. Opt. Express* **2** 385–96
- Read M, Reddick R L, Bode A P, Bellinger D A, Nichols T C, Taylor K, Smith S V, McMahon D K, Griggs T R and Brinkhous K M 1995 Preservation of hemostatic and structural properties of rehydrated lyophilized platelets: potential for long-term storage of dried platelets for transfusion *Proc. Natl Acad. Sci. USA* **92** 397–401
- Sanz J and Fayad Z A 2008 Imaging of atherosclerotic cardiovascular disease *Nature* **451** 953–7
- Sato Y, Hatakeyama K, Yamashita A, Marutsuka K, Sumiyoshi A and Asada Y 2005 Proportion of fibrin and platelets differs in thrombi on ruptured and eroded coronary atherosclerotic plaques in humans *Heart* **91** 526–30
- Urban M W, Chen S and Greenleaf J F 2008 Harmonic motion detection in a vibrating scattering medium *IEEE Trans. Ultrason. Ferroelectr. Freq. Control* **55** 1956–74
- White J G, Krumwiede M D and Escobar G 1999 EDTA induced changes in platelet structure and function: influence on particle uptake *Platelets* **10** 327–37
- Zerda A, Liu Z, Bodapati S, Teed R, Vaithilingam S, Khuri-Yakub B T, Chen X, Dai H and Gambhir S S 2010 Ultrahigh sensitivity carbon nanotube agents for photoacoustic molecular imaging in living mice *Nano Lett.* **10** 2168–72